AIAA Journal
Vol. 47, No. 10, October 2009

Analysis of Ultraviolet Radiation Predictions from High Altitude Two-Phase Plumes

Natalia E. Gimelshein,* Robert B. Lyons,† James G. Reuster,† and Sergey F. Gimelshein*
ERC, Inc., Edwards Air Force Base, California 93524

DOI: 10.2514/1.44067

Numerical study of a 5900-lb solid propellant thruster plume at an altitude of 118 km is performed using a combined multistep continuum/kinetic approach. The Navier–Stokes equations are solved for the flow inside the nozzle and the first several meters into the plume. The direct simulation Monte Carlo method is used to simulate the remaining plume and the plume-free stream interaction. A Monte Carlo based radiation code is applied in an overlay mode to calculate ultraviolet radiation in the near and far field of the plume. The computations take into account both alumina particles and soot. The effect of alumina particle emissivities and size distribution, as well as soot concentration, on ultraviolet radiation is clarified. Comparison of numerical results with available ultraviolet measurements is conducted.

I. Introduction

THE success of missile signature analysis depends heavily on the reliability of signature predictions for all stages of the boost trajectory. Prediction reliability, in turn, is significantly hampered by a large number of uncertainties and unknowns currently associated with the physics and gas dynamics of rocket propulsion system exhaust plumes interacting with the surrounding atmosphere. An essential feature of solid propellant rocket plumes that complicates flow analysis is related to the formation of particulates of varying types, sizes, and loadings. This makes rocket plume flows two phase, with one phase consisting of gas atoms and molecules and the other composed of nano- and microscale particulates. Disregard of the two-phase character of rocket plumes usually results in unacceptable loss in prediction accuracy. The specifics of interaction between the two phases and its impact on signatures and contamination depends on the propellant composition and thruster operation. The main particulate types are soot, propellant droplets, and aluminum oxide particles. The large mass fractions of aluminum oxide particles have a significant impact on the gas flow inside the nozzle (and therefore thruster performance), the near-field plume structure, and the far-field plume-atmosphere interaction structure. The strong influence from these particles on the flow structure inside the nozzle and in the plume results in a dramatic effect on radiation signatures.

There are a number of physical processes and quantities that affect radiation from rocket plumes in the UV region; most are associated with various particulate properties and propellant/motor parameters. In the related previous work [1], one of these processes was considered in detail, namely, photon scattering on alumina particles in a Star-27 motor plume at 118 km. The numerical results were compared with available on-board flight measurements [2] for two lines of sight; near field (4 deg from the plume axis) and far field (25 deg). It was shown that the main process determining the far-field radiation is photon scattering on submicron particles. Accounting for this effect increases the predicted radiance by a factor of 300, and the value of the full radiance at 230 nm in this case was approximately a factor of 4 lower than the measurements. The predicted near-field radiation was only about 30% higher than the measurements at 230 nm. This difference increases to an order of magnitude at 400 nm.

The main goal of this work, that is a continuation of [1], is to analyze possible processes for the difference between computed and experimental results, at both inband and spectral levels. Modeling of these processes uses engineering judgment to define reasonable bounds for the parameters of each process. Similar to [1], a multistep continuum-kinetic approach is used. Continuum Navier–Stokes solvers, VIPER and CFD++, are used to predict the flow inside of the nozzle and in the near field of the plume, respectively. A kinetic direct simulation Monte Carlo (DSMC)-based solver, SMILE, is used in the mid- and far fields of the flow. The final flow solution is obtained through successive application of these solvers from the inside of the nozzle to the outside, with the information transferred through boundary conditions (starting surfaces). Finally, a Monte Carlo radiation code NEMO is applied to calculate UV radiation.

The following important factors are examined.

1) The impact of soot particles on spectra in the far field: Soot particles, common to both hydrocarbon and solid propellant systems [3], do not significantly affect the plume gas flow due to their small concentrations, but are of interest due to their possible influence on radiation signatures. Soot particles are included in the present simulations in addition to the alumina particles considered previously, and the effect of their loading and size distribution is clarified later. Another possible source of small particulates in the plume, related to the homogeneous and heterogeneous condensation processes, is not considered in this work.

2) Alumina particle emissivities: There are a number of particle material properties that may potentially impact the gas and particle parameters in the plume. One of the most important properties related to radiation signatures is particle emissivity. Particle emissivity can be accurately calculated for spherical particles using the Mie theory, provided the complex index of refraction is defined as a function of temperature and wavelength. Comparison of the complex index of refraction deduced from available experimental data shows differences of up to 2 orders of magnitude observed between similar experiments. Because the real part of the refraction index is nearly constant and much larger than the imaginary part, this 2 orders of magnitude difference in the imaginary part translates to a 2 orders of magnitude difference in particle emissivities. In the present work, existing theoretical and empirical correlations for the particle refraction index are analyzed, and the sensitivity of radiation signatures from a Star-27 motor to particle emissivities is examined.

3) Alumina particle size distribution: Experimental evidence [4] indicates the presence of a substantial number of submicron particles in solid propellant rocket plumes. The size distribution of submicron particles exhibits substantial variability for different motor designs [3,4]. A submicron particle size distribution for the Star-27 motor

---

Presented as Paper 4120 at the 40th Thermophysics Conference, Seattle, Washington, 23–26 June 2008; received 27 February 2009; revision received 27 May 2009; accepted for publication 29 May 2009.

*Consultant.

†Senior Aerospace Engineer, Propulsion Directorate.

has not been measured to the authors' knowledge, and so three models were developed to test the sensitivity of UV emissions to the assumed size distribution. The three distributions span 4 orders of magnitude in assumed mass fraction for 0.2 μm diameter particles. This range of particle sizes tests the importance of small alumina particle scattering on the 25-deg model data comparisons.

II. Flow Conditions

Availability of detailed in-flight measurements of UV radiation from second and third stage plumes of the Strypi XI rocket provides a solid basis for numerical model testing and validation [5]. These measurements were conducted during the Bow Shock Ultraviolet 2 Experiment flown in early 1991. As part of this experiment, inband and spectrally resolved radiation from the Antares II motor (second stage) and the Star-27 motor (third stage) in the range from 200 to 400 nm were recorded for flight altitudes from approximately 104 to 119 km. For data collection, aft-viewing photometers and spectrometers installed on extractable periscopes were used. Two lines of sight were examined, 4 and 25 deg from the rocket centerline.

In this work, the point of the flight trajectory that has been numerically examined corresponds to the Star-27 steady-state operation at an altitude of 118 km. The geometric setup used to approximate experimental conditions is shown in Fig. 1. The freestream temperature and density are 330 K and 5.21×10^{17} molecule/m^3, and the atmosphere species mole fractions are 66.7% N_2, 7.6% O_2, and 25.7% O. The rocket moves with velocity of 2850 m/s. Zero angle of attack was assumed in the computations. This is reasonable because the experiments were conducted at angles of attack of less than 10 deg, and the influence of the angle of attack on the radiation at these altitudes is believed to be negligible. The nozzle thrust is about 5900 lb. The exhaust gas composition is listed as follows: $CO = 0.2225$, $CO_2 = 0.0291$, $Cl = 8.67 \times 10^{-3}$, $H = 0.0190$, $H_2 = 0.2734$, $H_2O = 0.1767$, $HCl = 0.1590$, $OH = 5.38 \times 10^{-4}$, and $N_2 = 0.1108$.

Three alumina particle size distributions are considered, all of them combining to the total mass fraction of the alumina particles in the exhaust of 29.5%. The first distribution is a 5 particle bin distribution used in the previous work [1], with the mass fraction of submicron, 0.2 μm diameter, particles of 0.15 relative to the total alumina mass fraction. The second, 14 particle bin distribution, uses the same combined submicron particle mass fraction of 0.15, but the number of submicron particle bins is 11 and not 1. Note that the amount of submicron particles in these distributions qualitatively agrees with the results of [6]. The third, 15 particle bin, distribution is based on the Worster [7] particle size model. The Worster distribution produced the smallest mass fractions for the submicron particles. The alumina particle mass fractions for these three distributions are shown in Fig. 2.

Two different mass fractions of soot particles were considered, 0.3 and 3% of the total propellant mass. The distribution of soot particle sizes was represented by three bins, 40, 100, and 200 nm. All bins are assumed to have one-third of the total soot mass fraction. This soot size distribution was used for all three alumina particle size distribution cases.

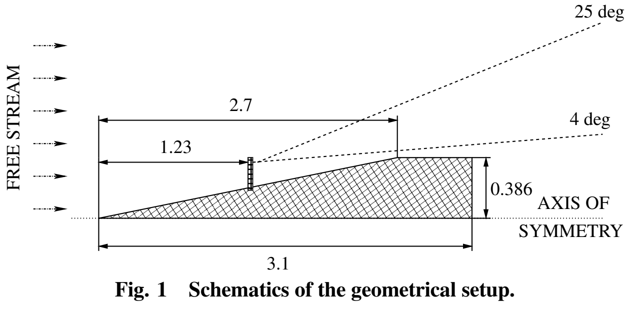

Fig. 1 Schematics of the geometrical setup.

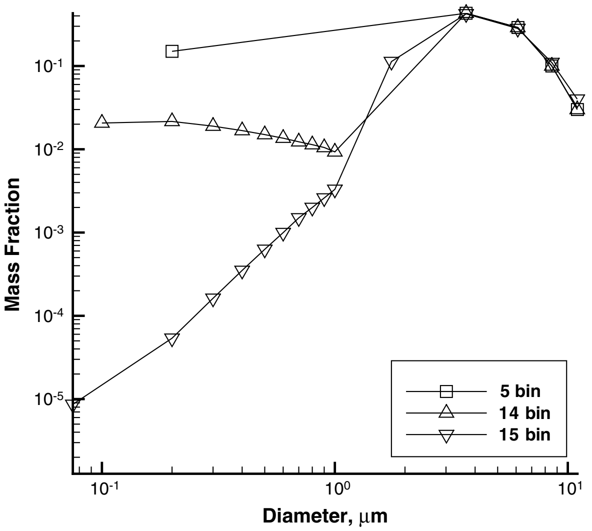

Fig. 2 Three particle size distributions.

III. Numerical Approaches

A multistep numerical approach is used for modeling the Star-27 rocket plume. A detailed description of the approach and accuracy-related issues is given in [1]. Only a brief outline is presented below.

Step 1: flow inside the nozzle. An axisymmetric parabolized Navier–Stokes (PNS) code VIPER [8,9] is used that includes finite rate gas chemistry, multiphase capability (via a two-way coupled Lagrangian method), and a variety of mostly empirical models for gas-particulate interaction and particulate evolution phenomena. The PNS scheme is applied from the sonic line near the throat of the nozzle to the exit plane of the nozzle. The combustion chamber pressure and temperature were assumed to be 34.3 atm and 3450 K, respectively.

Step 2: plume near field. An unstructured, chemically reacting, multiphase, turbulent, Reynolds averaged Navier–Stokes code CFD ++ [10,11] is applied with the macroparameters at the nozzle exit obtained at step 1 used as the plume inflow boundary conditions. A fully implicit, second order in space, Harten–Lax–van Leer, contact discontinuity Riemann approximation algorithm and a modified two equation k-ϵ turbulence model are used. An Eulerian based Henderson drag coefficient model [12] is used for the gas-particle flow interactions. All the 2-D axisymmetric grids used a baseline mesh of approximately 50,000 quadrilateral nodes.

Step 3: plume far field. A DSMC-based computational tool SMILE [13] is chosen to model the plume far field, with a starting surface at about 2 m from the nozzle exit plane obtained using CFD ++. The majorant frequency scheme [14] was used to calculate intermolecular interactions. The intermolecular potential was assumed to be a variable hard sphere [15]. Energy redistribution between the internal and translational modes was performed in accordance with the Larsen-Borgnakke model [16]. Temperature-dependent relaxation numbers were used. To achieve adequate numerical accuracy, multidomain DSMC computations were performed, with a combined 44 million simulated molecules and 12.5 million collision cells.

To analyze the impact of the alumina particle emissivity and size distribution, four different cases are considered for the flow outside the nozzle.

Case 1: 5 bin distribution of alumina particles with emissivities computed using [17].

Case 2: 5 bin distribution of alumina particles with emissivities computed using [18].

Case 3: 14 bin distribution of alumina particles with emissivities computed using [18].

Case 4: 15 bin distribution of alumina particles with emissivities computed using [18].

Step 4: radiation computation. The UV radiation is calculated in an overlay mode using the flow solutions obtained at previous steps. A parallel Monte Carlo radiation code, NEMO, developed at ERC that has 2-D and 3-D modules and generally allows for prediction of radiation from two-phase rocket plumes in the UV, visible, and infrared (IR) ranges was used. To calculate the emissivity of alumina and soot particles, it is necessary to know optical properties of the corresponding materials. The real part of the complex refraction coefficient of alumina particles was calculated using the expression given in [19]. The imaginary part was calculated using two different sets of expressions, the (i) set of [17], and the (ii) set of [18]. When calculating the absorption index according to [18], to provide for a smooth transition between the fundamental absorption and the Urbach edge absorption, a term $b\lambda_{\mathrm{opt}}$ was added to the expression for the fundamental absorption, similar to [17]. Both [17,18] used measurements to define the absorption coefficients. The differences between the two curves shown in Fig. 3 are attributed to different sample preparation techniques, which lead to different impurity levels and different absorption index values. Further research on the link between impurities and absorption index is needed. For soot, the complex refraction index was calculated according to [20]. Once the optical properties of the materials in the temperature and wavelength ranges of interest (300–3000 K and 0.2–20 μm, respectively) were calculated, the absorption efficiency Q_{abs} was calculated for the given particle radii using the BHMIE code first published in [21]. Then, the particle emissivity ϵ was obtained as

$$\epsilon = \int_{\lambda_{\min}}^{\lambda_{\max}} Q_{\mathrm{abs}} E_{b\lambda} \mathrm{d}\lambda / \sigma T^4 \tag{1}$$

where $E_{b\lambda}$ is the blackbody emissive power, σ is the Stefan-Boltzmann constant, $\lambda_{\min} = 0.2\ \mu$m, and $\lambda_{\max} = 20\ \mu$m.

The two different sets of expressions result in significant differences in the absorption index for the range of temperatures important in this work, as illustrated in Fig. 3 (left). Note that the newer data set is characterized by a much lower absorption index for higher wavelengths, which is expected to strongly impact the UV spectra. The difference is also reflected in particle emissivities computed with these sets. Figure 3 (right) shows emissivities for 0.2 and 3.66-μm diam particles as a function of surface temperature, calculated using [17,18]. As expected, the emissivity is much higher for bigger particles. The temperature dependence is similar for both diameters. For the model of [17], the emissivity stays approximately constant until the temperature reaches ∼1750 K, and then grows rapidly. For the model of [18], the emissivity starts growing after 2000 K. In the 2000–3000 K temperature range, the emissivity predicted by model [17] is much higher than both liquid and γ-phase emissivities predicted by the model [18].

IV. Results and Discussions

A. Gas Properties in the Plume

The flowfields that illustrate gas properties from the nozzle exit to 2.5 km downstream are given in Fig. 4. The three overlapping domains here illustrate the multizone DSMC approach used in this work (each successive zone uses the solution from the previous zone for the inflow boundary condition). The translational temperature field clearly shows the increase in temperature in the mixing layer between the plume and the freestream. Note that the 25 deg line of sight of the far-field photometer intersects with the elevated temperature region at about 500 m from the nozzle. The translational temperature in that region is about 1000 K, which should not have any implications for UV radiation, except for possible evaporation of condensed liquid droplets (that are not accounted for in this work). Typical for plumes expanding in a background gas, the compression region produced by the interaction of the freestream and the plume converges to the nozzle axis at some distance from the nozzle. In this case, this distance is over 1 km, as the Mach number field clearly shows. The Mach number at the nozzle axis reaches its minimum of about 5 at about 1400 m from the nozzle. The maximum Mach number of about 30 is observed in the expanding plume at $X \approx 600$ m.

Although the mean free path in the freestream is large, and the Knudsen number based on the rocket length of 3.1 m is about 1, the flow in the mixing layer, which is hundreds of meters wide and kilometers long, is near continuum. This is illustrated in Fig. 4 (bottom) where the gas mean free path is plotted. Generally, this makes conventional continuum solvers applicable in that region. However, there is an expansion region in the core flow where the gas mean free path continues to increase, reaching its maximum of about 40 m. The radius of the plume core flow varies from 100 to 200 m, which is comparable to the gas mean free path there. The applicability of continuum approaches in that region may therefore be questionable.

B. Alumina Particle Properties in the Far Field

Comparison of gas flowfields obtained for different alumina particle emissivities and particle size distributions have shown that the effect of these properties on gas in the far field of the plume is relatively small. The maximum difference observed between cases 1 and 4 amounted to about 5% for gas temperature, and still smaller for gas densities. As expected, the largest effect of particle properties is seen in particle surface temperatures. The comparison of the most important property in terms of UV radiation, namely, the surface temperature of 3.66 μm alumina particles, is presented in Fig. 5. Note that the steplike plume boundary in the far-field DSMC domain is due to the finite macroparameter cell size.

The upper two plots illustrate the impact of the particle emissivity. The values of the emissivity in case 1 are up to an order of magnitude larger than those in case 2. This results in much faster cooling of particles. For case 1, the particle surface temperature decreases to the critical value of 2100 K at 55 m from the nozzle exit. For case 2, it takes particles over 400 m to reach this temperature. After the crystallization begins, for both cases the temperature reaches the alumina melting temperature of 2320 K. This value is reached at about 500 m for case 2 instead of 60 m for case 1. One may expect

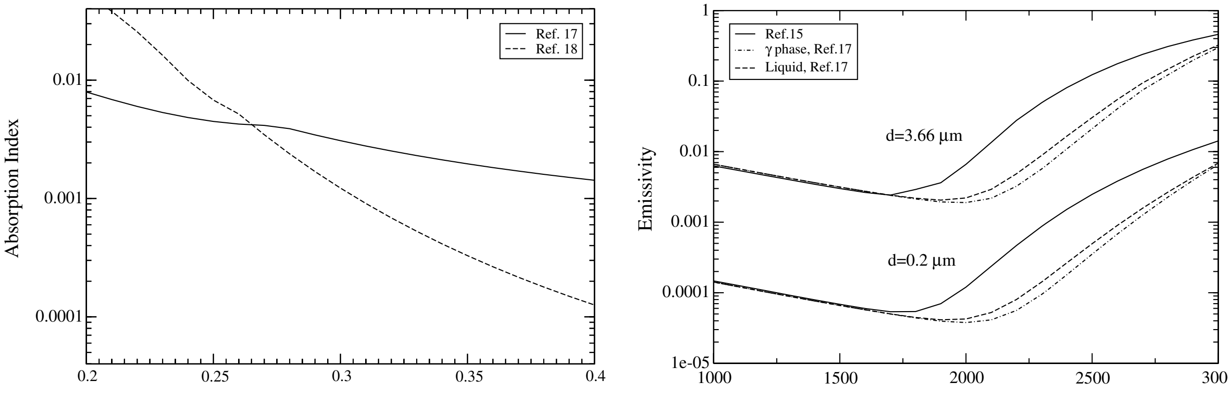

Fig. 3 Alumina absorption index calculated with two different sets of expressions, [17,18] (γ phase), for a surface temperature of 2200 K (left). Emissivities for two particle diameters computed with these two sets (right).

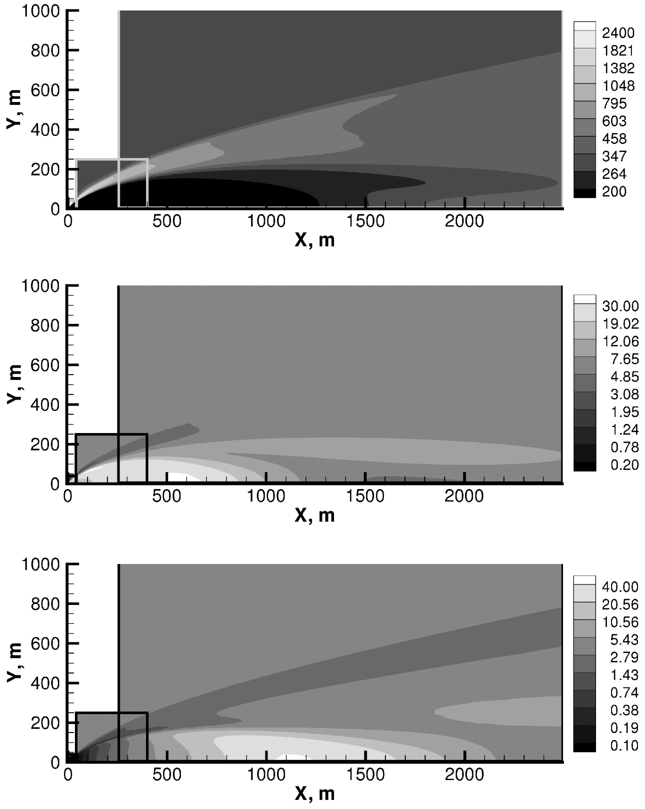

Fig. 4 Plume translational temperature in Kelvin (top), Mach number (middle), and gas mean free path (bottom) in meters.

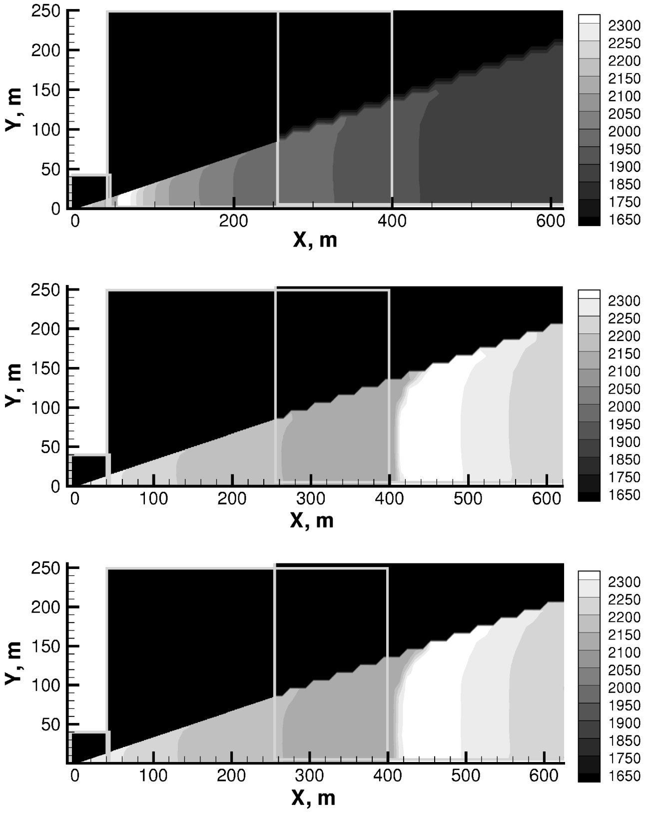

Fig. 5 Surface temperature field of 3.66 μm particles for case 1, top; case 2, middle; and case 3, bottom.

larger effects of the phase change for case 1 than for case 2, because particle densities are very small at 500 m. The influence of the size distribution on the particle surface temperature is negligibly small compared to that of particles emissivities for both large and small particles (compare Fig. 5, middle and bottom). Case 4 is practically identical to case 3, and is not shown here.

Finally, the density of submicron particles in the far field is presented in Fig. 6 for case 2 (the other cases are qualitatively similar). As follows from the near-field results presented previously, there is a large number of submicron particles in the field of view of the 25 deg photometer. This, along with high temperature of large particles in the far field, means that the contribution of the far-field submicron particles on the radiance detected by the 25 deg instrument may be important and needs to be analyzed. However, the temperature of these particles does not change much in the far field and stays at around 1000 K, which is too low for significant UV emission.

C. Soot Particle Properties in the Far Field

The properties of soot in the plume are now examined. Although only case 1 is shown here, the soot properties for the other three cases are very similar. The number density of 100-nm soot particles is shown in Fig. 7 (left). Similar to submicron alumina, a large amount of soot reaches the field of view of the 25 deg photometer. Light and small soot particles to a large extent follow the gas streamlines in the near field, although they then deviate slightly from gas streamlines in the far field. The gas in the far field is too rarefied to significantly affect the soot temperature, although there is a visible increase in temperature at larger angles from the plume axis, where the soot particles interact directly with the freestream. Even though the soot emissivities are much higher than those of the same-sized alumina particles, low soot temperatures preclude soot from being a direct contributor to the UV emission; only scattering processes are important.

The number density profiles of soot particles along the line of sight of the 25 deg photometer are given in Fig. 8. Very few particles are near the instrument. Note here that the values in the first few centimeters may actually be even lower if soot particles were modeled inside the nozzle, and not just assumed to follow the gas streamlines there. Still, it is believed to be a minor factor in terms of the actual contribution of soot particles in photon scattering, especially keeping in mind the uncertainties in the soot formation and distribution. The soot density reaches its maximum at about 8 m from the detector, and then decreases almost linearly (in log scale) in the far field. There is some deviation from linearity for smaller particles that is attributed to the impact of the freestream on soot particle trajectories.

D. UV Radiance at 4 and 25 deg

The availability of experimental data [5] allows quantitative analysis of the impact of different factors mentioned previously on the radiation intensity. The spectral radiance at 230 nm is presented in Table 1 for four numerical cases under consideration, along with the experimental results [5]. Two photometer lines of sight are considered, 4 and 25 deg. Consider first the near-field 4 deg results. A significant decrease in particle emissivities, illustrated in the comparison of cases 1 and 2, results in an about 20% increase in radiance. This is related primarily to the fact that the temperature of large (micron-sized) particles in the plume decreases much slower for case 2. The higher temperatures cause more photons to be emitted, even though the emissivities are lower. It is interesting to note that there is a further

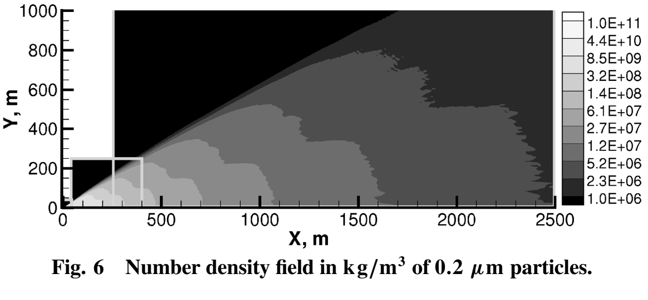

Fig. 6 Number density field in $\mathrm{kg/m^3}$ of 0.2 μm particles.

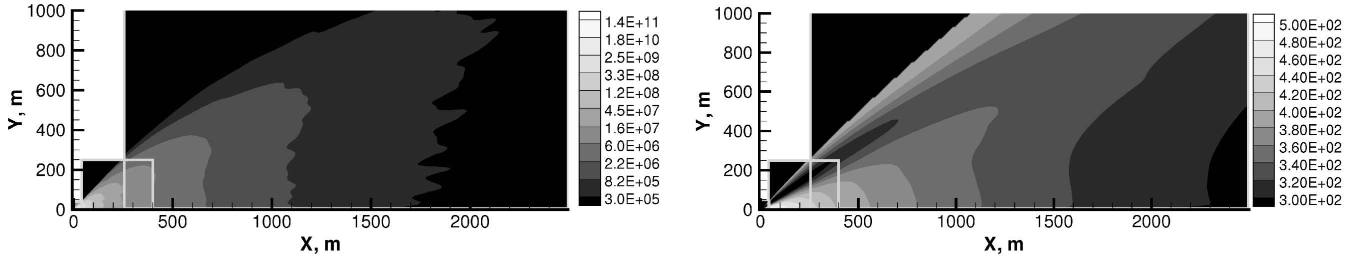

Fig. 7 Number density in particle/m^3 (left) and surface temperature in Kelvin of 0.1 μm diameter soot particles.

increase in the radiation when more submicron particle bins are included in the computations (compare cases 2 and 3). The reason for this is photon scattering on small particles. The large number of 0.2 μm particles in case 2 results in a significant reduction in radiation due to scattering. When the radiation is computed without submicron alumina particle bins, the radiance values for cases 2 and 3 are almost the same (8.3×10^{-6} W/μm m^2 sr for case 3 against 8.4×10^{-6} W/μm m^2 sr for case 2), because the number density and surface temperature of large particles for these two cases are almost identical. The larger number of micron-sized particles and small number of submicron-sized particles result in a smaller impact from scattering and the highest radiation for case 4.

All numerical values for the 4 deg photometer are noticeably larger than the measured radiation of 3.6×10^{-6} W/μm m^2 sr. This is primarily attributed to the impact of the gas-particle heat transfer model. Previous analysis [22] has shown that the heat transfer model implemented in CFD++ is reproduced closely by the free molecular model with the energy accommodation coefficients of about 0.4. A model with more efficient heat transfer (larger energy accommodation coefficient) will cool particles inside the nozzle more effectively, and thus the radiative emission would decrease. Another reason is the likely underprediction of the number of submicron particles in the numerical simulation, as discussed next.

The results given in Table 1 show that the radiation computed along the 25 deg line of sight is significantly lower than the measured value. The maximum radiation, recorded for case 3, is almost 3 times lower than the data. As all the radiation comes to the 25 deg detector due to the scattering on submicron particles [1], it is clear that the model underpredicts the amount of these particles in the plume. The formation of a somewhat larger number of submicron alumina particles is possible, as well as larger soot concentrations in the exhaust. Note also that the current work included only two out of four possible sources of submicron particles, aluminum oxidation and soot formation. The other two, heterogeneous and homogeneous condensation and nozzle surface degradation, are not modeled.

Table 1 Radiation at 230 nm for different models, W/μm m^2 sr. 0.3% soot is included

Case	4 deg	25 deg
1	4.85×10^{-6}	3.55×10^{-9}
2	5.75×10^{-6}	6.20×10^{-9}
3	6.99×10^{-6}	7.70×10^{-9}
4	9.45×10^{-6}	2.28×10^{-9}
Experiment	3.6×10^{-6}	22.0×10^{-9}

Table 2 Effect of soot particles on radiation at 230 nm, case 2, W/μm m^2 sr

Line of sight	Soot content	Radiance
25 deg	No soot	4.83×10^{-9}
25 deg	40 nm bin only	5.21×10^{-9}
25 deg	40 and 100 nm bins	5.92×10^{-9}
25 deg	All soot bins	6.20×10^{-9}
25 deg	3% soot	17.7×10^{-9}
4 deg	No soot	5.75×10^{-6}
4 deg	3% soot	5.62×10^{-6}

An assessment of condensation's potential impact on the results was conducted. The calculation of the water supersaturation ratio has shown that the condensation will start at about 10 m from the nozzle exit for the 25 deg line of sight and 20 m for the 4 deg line of sight, because of the significant decrease in gas temperature. The analysis of collision rates in the plume provides the upper estimates for the water cluster sizes in the plume (sticking is assumed to be unity and no evaporation is allowed), which are about 1200 monomers per cluster. It is clear that the size of such clusters is too small to be a significant factor in UV photon scattering. The heterogeneous condensation on HCl molecules is also not expected to be a major factor for UV radiation signatures. The impact of another source of submicron particles, nozzle surface degradation, is expected to be well below 1% due to their relatively small number.

The impact of soot particles in the plume on the spectral radiation at 230 nm is shown in Table 2. The results indicate that the inclusion of 0.3% soot results in a 25% increase in radiation in the far field for case 2 (the results for case 3 are similar, whereas for case 4 the photons reflected on soot particles constitute about two-thirds of the total radiation at 25 deg). It is important to note that all three bins of soot particles (even the smallest bin of 40 nm) contribute noticeably to the far-field radiation. The increase of soot mass loading in the plume from 0.3 to 3% results in a drastic increase in the far-field radiation, with the 25-deg line of sight radiation being only about 20% lower than the data (although such a high mass loading of soot does not seem very likely). The near-field radiation, that does not change much for the 0.3% soot case, decreases about 2% for the 3% soot case.

In addition to the uncertainties related to the gas-particle heat transfer and particle size distribution, that both influence the agreement between the experimental and numerical data, there is also an uncertainty related to the accuracy of the line of sight value determination. The actual value may somewhat differ from the reported 4 and 25 deg, and a small difference in the line of sight results in a noticeable difference in the radiation prediction, as indicated in Table 3. Relatively large numbers of submicron particles in the far field raise the question of convergence of the obtained results in terms of the length of the computational domain. To prove the convergence, the radiation calculations have been conducted with varying domain length (in all runs only the downstream boundary was moved). The results for the 25 deg line of sight are presented in Fig. 9. The main conclusion here is that the radiation shows minimum change after the first few hundred meters downstream from the nozzle axis. Note that the near-field radiance converges even faster. That means that the DSMC modeling of the plume near and midfields only, without the far field, would provide adequate accuracy for radiation predictions.

Table 3 Effect of the line of sight value on radiation at 230 nm, case 2, W/μm m^2 sr

3.0	7.43×10^{-6}	24.0	9.18×10^{-9}
3.5	6.57×10^{-6}	24.5	7.60×10^{-9}
3.9	5.89×10^{-6}	24.9	6.47×10^{-9}
4.0	5.75×10^{-6}	25.0	6.20×10^{-9}
4.1	5.58×10^{-6}	25.1	5.95×10^{-9}
4.5	5.07×10^{-6}	25.5	5.06×10^{-9}
5.0	4.60×10^{-6}	26.0	4.09×10^{-9}

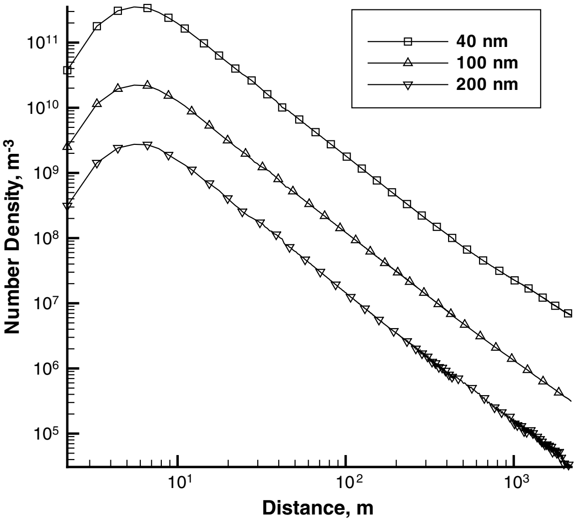

Fig. 8 Soot number density along the 25 deg line of sight.

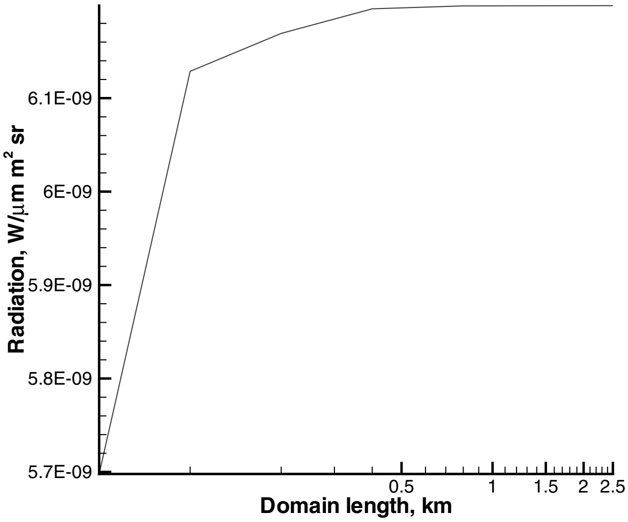

Fig. 9 The impact of the far field on the total radiance at 230 nm, case 2.

Previous results [1] have shown a qualitative difference in the shape of the UV spectra from the published data. Although the agreement was reasonable (within a factor of 2) for the 200–300 nm range, at 400 nm the numerical results overpredicted by a factor of 20. This was attributed mostly to the influence of alumina particle emissivities (the absorption index of [17] was used in [1]). Similar to the previous results, the computed spectral shape is much steeper than the experimental one when the emissivities based on [17] are used, as illustrated in Fig. 10, case 1. The emissivities computed from [18], however, allow one to capture the shape of the experimental spectra much closer (cases 2–4).

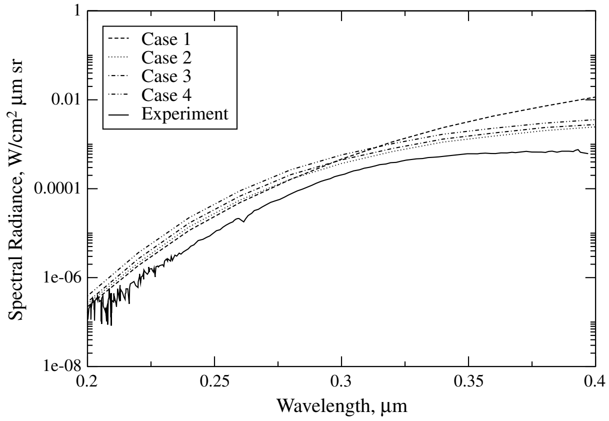

Fig. 10 Comparison of spectral radiance for different cases with experimental data.

V. Conclusions

A computational study of a Star-27 solid propellant rocket plume at an altitude of 118 km has been conducted using a combined multistep continuum/kinetic approach. The solution of the Navier–Stokes equations was obtained inside the nozzle and in the plume in the vicinity of the nozzle exit. The DSMC method was used to simulate most of the plume, as well as the plume-free stream interaction. A Monte Carlo based radiation solver was used in an overlay mode to calculate UV radiation in the plume. All gas dynamic flow solvers used in this work included two-way coupling between the gas flow and particles, with two types of particles being considered, alumina and soot.

The impact of alumina particle emissivities on particle properties and UV radiation in the near and far fields has been analyzed. It has been shown that the use of emissivities based on [18] results in much lower particle temperatures in the plume and significant delay of the liquid-to-γ phase change, as compared to the case when emissivities based on [17] are used. The radiation was found to be tens of percent higher both in the near and far fields when smaller values of emissivities are used due to slower particle cooling. The effect of particle emissivities on the gas is relatively small. Comparison with available experimental data have shown that the model overpredicts the experimental data in the near field (4 deg line of sight) by on average a factor of 2, which is thought to be the effect of the gas-particle heat transfer model inside the nozzle.

The numerical results for the far-field (25 deg line of sight) UV radiation underpredict the measurements, with the difference ranging from almost a factor of 10 to about 25%, depending on the submicron alumina particle size distribution and soot mass loading. Both these factors are not well known, and were therefore parameterized. Hot micron-sized particle emission in the plume core flow scattered on submicron particles in the side flow is the dominant source of the far-field UV radiation, and both the alumina particles and soot were found to significantly contribute to the scattering process. The effect of condensation and nozzle surface erosion on the UV photon scattering was estimated to be relatively small. Both far- and near-field radiation prediction were found to be sensitive to the accuracy of the line of sight determination.

Acknowledgments

The work at University of Southern California was supported in part by the Propulsion Directorate of the U.S. Air Force Research Laboratory at Edwards Air Force Base, California. The authors are thankful to Ingrid Wysong and Thomas Smith for many fruitful discussions.

References

[1] Gimelshein, N., Lyons, R., Reuster, J., and Gimelshein, S., "Numerical Prediction of UV Radiation from Two-Phase Plumes at High Altitudes," *AIAA Journal*, Vol. 46, No. 7, 2008, pp. 1764–1772. doi:10.2514/1.34762

[2] Erdman, P. W., Zipf, E. C., Espy, P., Howlett, C., Collins, R. J., Cristou, C., Levin, D. A., and Candler, G. V., "In-Situ Measurements of UV and VUV Radiation from a Rocket Plume and Ee-Entry Bow-Shock," AIAA Paper 91-0124, 1991.

[3] Reed, R., and Calia, V., "Review of Aluminum Oxide Rocket Exhaust Particles," AIAA Paper 93-2819, 1993.

[4] Schmid, O., Reeves, J., Wilson, J., Wiedinmyer, C., Brock, C., Toohey, D., Availlone, L., Gates, A., and Ross, M., "Size-Resolved Particle Emission Indices in the Stratospheric Plume of an Athena II Rocket," *Journal of Geophysical Research*, Vol. 108, No. D8, 2003, pp. AAC6.1–AAC6.8. doi:10.1029/2002JD002486

[5] Smathers, H. W., Horan, D. M., Cardon, J. D., Malaret, E. R., Singh, M., Sorensen, T., Laufer, P. M., Corson, M. R., Brandenburg, J. E., McKay, J. A., and Strunce, R. R., "Ultraviolet Plume Instrument Imaging from the LACE Satellite Strypi Rocket Plume," Naval Research Laboratory Rept. NRL/FR/8121-93-9526, Washington, D.C., Sept. 1993.

[6] Gosse, S., Hespel, L., Gossart, P. and Delfour, A., "Morphological Characterization and Particle Sizing of Alumina Particles in Solid Rocket Motor," *Journal of Propulsion and Power*, Vol. 22, No. 1, 2006, pp. 127–135.
doi:10.2514/1.13626

[7] Lyons, R., Wormhoudt, J., and Kolb, C., "Calculation of Visible Radiation from Missile Plumes," AIAA Paper 81-1111, 1981.

[8] Simmons, F. S., *Rocket Exhaust Plume Phenomenology*, The Aerospace Corporation Aerospace Press Series, AIAA, Reston, VA, 2000, p. 286.

[9] Kawasaki, A. H., Coats, D. E., and Berker, D. R., "A Two-Phase, Two-Dimensional, Reacting Parabolized Navier-Stokes Solver for the Prediction of Solid Rocket Motor Flowfields," AIAA Paper 92-3600, 1992.

[10] Chakravarthy, S., and Peroomian, O., "Some Internal Flow Applications of a Unified-Grid CFD Methodology," AIAA 96-2926, July 1996.

[11] Peroomian, O., Chakravarthy, S., and Golberg, U., "A 'Grid Transparent' Methodology for CFD," AIAA Paper 97-0724, 1997.

[12] Henderson, C. A., "Drag Coefficients of Spheres in Continuum and Rarefied Flows," *AIAA Journal*, Vol. 14, No. 6, June 1976, pp. 707–708.
doi:10.2514/3.61409

[13] Ivanov, M. S., Markelov, G. N., and Gimelshein, S. F., "Statistical Simulation of Reactive Rarefied Flows: Numerical Approach and Applications," AIAA Paper 98-2669, 1998.

[14] Ivanov, M. S., and Rogasinsky, S. V., "Analysis of the Numerical Techniques of the Direct Simulation Monte Carlo Method in the Rarefied Gas Dynamics," *Soviet Journal of Numerical Analysis Mathematical Modeling*, Vol. 3, No. 6, 1988, pp. 453–465.

[15] Bird, G. A., *Molecular Gas Dynamics and the Direct Simulation of Gas Flows*, Clarendon Press, Oxford, 1994, p. 458.

[16] Borgnakke, C., and Larsen, P. S., "Statistical Collision Model for Monte Carlo Simulation of Polyatomic Gas Mixture," *Journal of Computational Physics*, Vol. 18, 1975, pp. 405–420.
doi:10.1016/0021-9991(75)90094-7

[17] Anfimov, N. A., Karabadzhak, G. F., Khmelinin, B. A., Plastinin, Y. A., and Rodionov, A. V., "Analysis of Mechanisms and Nature of Radiation from Aluminum Oxide in Different Phase States in Solid Rocket Exhaust Plumes," AIAA Paper 93-2818, 1993.

[18] Plastinin, Y., Karabdzhak, G., Khmelinin, B., Baula, G., and Rodionov, A., "Ultraviolet, Visible and Infrared Spectra Modeling for Solid and Liquid-Fuel Rocket Exhausts," AIAA Paper 2001-0660, 2001.

[19] Dombrovsky, L. A., *Radiation Heat Transfer in Disperse Systems*, Begell House, New York, 1996.

[20] Lee, S. C., and Tien, C. L., "Optical Constants of Soot in Hydrocarbon Flames," *Proceedings of the Eighteenth International Symposium on Combustion*, The Combustion Institute, Pittsburgh, PA, 1981.

[21] Bohren, C. F., and Huffman, D. R. *Absorption and Scattering of Light by Small Particles* Wiley, New York, 1982, Appendix A.

[22] Gimelshein, S., Markelov, G., and Muylaert, J., "Numerical Modeling of Low Thrust Solid Propellant Nozzles at High Altitudes," AIAA 2006-3273, 5–8 June 2006.

T. Jackson
Associate Editor